Jet Geometry and Rate Estimate of Coincident Gamma-Ray Burst and Gravitationalwave Observations

Kentaro Mogushi ^{1,2} , Marco Cavaglià ^{1,2}, and Karelle Siellez ^{3,4}

¹ Physics Department, Missouri University of Science and Technology, 1315 N. Pine Street, Rolla, MO 65409, USA

Department of Physics and Astronomy, The University of Mississippi, University, MS 38677-1848, USA; kmhhz@umsystem.edu

³ University of Santa Cruz, Department of Astronomy and Astrophysics, 7487 Red Hill Road, Santa Cruz, CA 95064, USA

⁴ Georgia Institute of Technology, Center for Relativistic Astrophysics, 837 State Street, Atlanta, GA 30332, USA

**Received 2018 December 7; revised 2019 May 1; accepted 2019 May 4; published 2019 July 24

Abstract

Short gamma-ray burst (SGRB) progenitors have long been thought to be coalescing binary systems of two neutron stars (NSNS) or a neutron star and a black hole. The 2017 August 17th detection of the GW170817 gravitational-wave (GW) signal by Advanced LIGO and Advanced Virgo in coincidence with the electromagnetic observation of the SGRB GRB 170817A confirmed this scenario and provided new physical information on the nature of these astronomical events. We use SGRB observations by the Neil Gehrels Swift Observatory Burst Alert Telescope and GW170817/GRB 170817A observational data to estimate the detection rate of coincident GW and electromagnetic observations by a GW detector network and constrain the physical parameters of the SGRB jet structure. We estimate the rate of GW detections coincident with SGRB electromagnetic detections by the *Fermi* Gamma-ray Burst Monitor to be between \sim 0.1 and \sim 0.6 yr⁻¹ in the third LIGO-Virgo observing run and between \sim 0.3 and \sim 1.8 yr⁻¹ for the LIGO-Virgo-KAGRA network at design sensitivity. Assuming a structured model with a uniform ultrarelativistic jet surrounded by a region with power-law decay emission, we find the jet half-opening angle and the power-law decay exponent to be $\theta_c \sim 7^{\circ}$ -22° and $s \sim$ 5-30 at a 1 σ confidence level, respectively.

Key words: gamma-ray burst: general – stars: black holes – stars: jets – stars: neutron

1. Introduction

Gamma-ray bursts (GRBs) are extremely energetic electromagnetic (EM) events of astrophysical origin with prompt emission observed in the gamma-ray band. They are usually followed by an afterglow with energy ranging from the GeV to the radio band (Guelbenzu et al. 2012; Meszaros & Gehrels 2012). Observations show the existence of at least two classes of GRBs with distinct progenitors (Kouveliotou et al. 1993). Long GRBs (LGRBs) are characterized by a softer gamma-ray emission lasting typically over two seconds. Short GRBs (SGRBs) are characterized by a harder, shorter-lived emission. While LGRB progenitors are known to be core-collapse supernovae (Hjorth et al. 2003; Lee et al. 2004; Campana et al. 2006; Fruchter et al. 2006; Woosley & Bloom 2006), the origin of SGRBs was long thought to be the coalescence of binary systems of two neutron stars (NSNS) or neutron star and black hole (NSBH) mergers. The recent detection of the 2018 August 17th gravitational-wave (GW) signal called GW170817 by Advanced LIGO and Advanced Virgo in coincidence with the EM observation of the SGRB GRB 170817A (Abbott et al. 2017a, 2017b; Goldstein et al. 2017) confirmed the widespread hypothesis that at least some SGRBs indeed originate from NSNS mergers.

The LIGO Scientific Collaboration (LSC) and the Virgo Collaboration have built low-latency analysis pipelines that can promptly identify GW transient candidates (Nitz et al. 2017; Privitera et al. 2017). High-energy neutrino detectors and over 80 astronomical telescopes with observational capability ranging from gamma-rays to the radio band signed memoranda of understanding for the follow-up of GW detection candidates with the LSC and Virgo. Information about sky localization of a possible GW detection was distributed to these partners within a few minutes from the trigger identification (Branchesi

et al. 2012). In parallel, the LSC and Virgo performed GW searches triggered by EM GRB observations (Mandel et al. 2012). The results of the search for GW signals coincident with GRB observations by the Fermi Gamma-ray Burst Monitor (GBM; Atwood et al. 2009), the Neil Gehrels Swift Observatory (NGSO) Burst Burst Alert Telescope (BAT; Gehrels et al. 2004) and the multimission detections reported through the InterPlanetary Network (IPN; Frederiks 2013) during the first observing run of Advanced LIGO (2015 September 2 to 2016 January 19) were published in Abbott et al. (2017c) with no evidence of GW signals coincident with SGRBs. Results of these searches for the second Advanced LIGO-Virgo observing run are expected to be released soon. Starting with the third observation run, the LSC and the Virgo Collaboration release Open Public Alerts for GW transient event candidate detections.

Over the past few years, several studies have constrained the local rate density of NSNS and NSBH mergers and estimated the number of coincident observations between GW detectors and EM observatories (Guetta & Piran 2006; Coward et al. 2012; Petrillo et al. 2012; Siellez et al. 2014; Fong et al. 2015; Regimbau et al. 2015; Chruslinska et al. 2018). Estimates of the local rate density of NSNS and NSBH mergers are highly uncertain, ranging from \sim 10 to a few thousand events per year per cubic gigaparsec (Gpc). Coward et al. (2012) estimate a local rate density $\rho_G \sim 8-1800 \, \mathrm{Gpc}^{-3} \, \mathrm{yr}^{-1}$. Petrillo et al. (2012), Siellez et al. (2014), and Fong et al. (2015) find larger lower bounds with local rate densities in the range $\rho_G \sim 500-1500 \, {\rm Gpc}^{-3} \, {\rm yr}^{-1},$ $\rho_G \sim 92-1154 \, {\rm Gpc}^{-3} \, {\rm yr}^{-1},$ and $\rho_G \sim 90-1850 \, {\rm Gpc}^{-3} \, {\rm yr}^{-1},$ respectively. Guetta & Piran (2006) estimate a local rate density of $\rho_G \sim 8-30\,\mathrm{Gpc}^{-3}\,\mathrm{yr}^{-1}$. All the above studies are based on EM observational data. Population synthesis studies based on the Milky Way star formation rate predict NSNS observation rates in Advanced LIGO between $2~{\rm yr}^{-1}$ (Voss & Tauris 2003) and $6~{\rm yr}^{-1}$ (de Freitas Pacheco et al. 2006). Studies based on the observations of Galactic binary pulsars lead to rate estimates between $10\,\mathrm{yr}^{-1}$ (O'Shaughnessy et al. 2010) and $35\,\mathrm{yr}^{-1}$ (Kalogera et al. 2007). A recent investigation based on simulations of compact binary evolution predicts an NSNS local rate density of $48\,\mathrm{Gpc}^{-3}\,\mathrm{yr}^{-1}$ (Chruslinska et al. 2018). Null results of NSNS and NSBH merger observations in the first Advanced LIGO observing run give NSNS and NSBH merger upper bounds of $12,600\,\mathrm{Gpc}^{-3}\,\mathrm{yr}^{-1}$ and $3600\,\mathrm{Gpc}^{-3}\,\mathrm{yr}^{-1}$, respectively (Abbott et al. 2016). The NSNS merger rate estimate from the second observation run is between 340 and $4740\,\mathrm{Gpc}^{-3}\,\mathrm{yr}^{-1}$ (Abbott et al. 2017a).

The detection of the GW170817/GRB 170817A provides a new means of improving the above estimates and constraining the physical properties of SGRBs. The observed luminosity of GRB 170817A is lower than the observed luminosity of all SGRBs with known redshift by at least two orders of magnitude. This discrepancy could be explained by the existence of a subluminous population of SGRBs (Siellez et al. 2017) or by GRB 170817A being observed off-axis, i.e., at a large inclination angle. Abbott et al. (2017b) consider three possible scenarios for this paradigm: (1) the "uniform top-hat" model (Rhoads 1999), where the SGRB is described by a conical jet with uniform, relativistic emission, (2) the "cocoon" shock break-out model, where a quasi-isotropic emission is due to shocked material around a relativistic jet (Lazzati et al. 2018), and (3) a "structured jet" model, where a narrower ultrarelativistic jet is surrounded by a mildly relativistic sheath (Rossi et al. 2002; Zhang & Meszaros 2002; Kumar & Granot 2003; Granot 2007; Pescalli et al. 2015). Radio and X-ray counterpart observations provide some evidence that GW170817 may be viewed off-axis (Fong et al. 2017). Margutti et al. (2018) use post-merger optical observations by the Hubble Space Telescope, radio observations by the Very Large Array and X-ray observations by the *Chandra X-ray Observatory* to rule out the uniform top-hat model. The Very Long Baseline Interferometric (VLBI) detection of superluminal motion in GRB 170817A also supports this conclusion (Mooley et al. 2018). The recent study for 220-260 days post-merger rules out the cocoon model in favor of a structured jet model (Alexander et al. 2018). Jin (2017) estimate that the number of coincident GW–EM observations for a Gaussian-type structured jet (Zhang & Meszaros 2004) increase by a factor of ~16 w.r.t. a uniform

In this paper, we first use a catalog of SGRB observations by NGSO-BAT (Gehrels et al. 2004) with known redshifts to estimate the local rate density of NSNS and NSBH coalescences. We consider two different luminosity function (LF) models for the SGRBs, the Schechter LF (Andreon et al. 2006), and the broken power LF (Guetta & Piran 2006), as well as a number of different star formation rate functions (Cole et al. 2001; Porciani & Madau 2001; Hernquist & Springel 2003; Hopkins & Beacom 2006; Fardal et al. 2007; Wilkins et al. 2008). We then use the observational properties of GW170817/GRB 170817A to constrain the parameters of the structured jet model (Pescalli et al. 2015). Finally, we estimate the rates of GW events observable by a network of ground-based GW detectors and the rates of coincident GW-SGRB observations with EM partners.

2. Method

The number \mathcal{N} of SGRBs with known redshift that are *observed* by an EM instrument per unit observation time t,

redshift z, and absolute bolometric source-frame luminosity L at an inclination angle θ_o (the angle between the axis of the SGRB jet and the observer's line of sight) is

$$\mathcal{N}(t, z, L, \cos \theta_o) \equiv \frac{dN(t, z, L, \cos \theta_o)}{dt dz dL d(\cos \theta_o)}$$

$$= \frac{f}{1+z} \frac{dV(z)}{dz} \frac{dN_S(t', z, L, \cos \theta_o)}{dt' dV dL d(\cos \theta_o)}, \quad (1)$$

where N_S is the *actual* number of SGRBs with absolute luminosity L, inclination angle θ_o , and redshift z per unit comoving volume V, t' is the time in the SGRB local frame, and $f = f_x f_{\text{FOV}}$, where f_r is the fraction of observed SGRB with known redshift and f_{FOV} is the detector field of view. In writing Equation (1) we have assumed that the SGRBs are isotropically distributed and tacitly assumed axial symmetry around the SGRB axis. If the luminosity distribution of the SGRBs is independent from the SGRB formation rate, Equation (1) can be rewritten as

$$\mathcal{N} = \rho_s \frac{f}{1+z} \frac{dV(z)}{dz} R_S(t', z) \frac{dN_{S'}(z, L, \cos \theta_o)}{dL d(\cos \theta_o)}, \tag{2}$$

where R_S is the SGRB rate function (RF), i.e., the number of SGRBs per unit source time and comoving volume, and ρ_S is a proportionality constant. We assume that R_S is independent of t' and normalize R_S and $N_{S'}$ as

$$R_S(0) = 1, \quad \int_{-1}^1 d(\cos \theta_o) \int_0^\infty dL \frac{dN_{S'}}{dL d(\cos \theta_o)} \bigg|_{z=0} = 1.$$
 (3)

With these normalizations, the constant ρ_S in Equation (2) is the local rate density, i.e., the number of SGRBs per unit volume per unit time in the local universe:

$$\rho_S = \frac{1}{f} \frac{dN}{dt dV} \bigg|_{z=0} . \tag{4}$$

The number of SGRBs with known redshift up to z that are observed by a given EM detector during the observation time T_o is

$$N(z) = T_o f \rho_S \int_0^z dz' \frac{1}{1+z'} R_S(z') \frac{dV(z')}{dz'} \times \int_{-1}^1 d(\cos\theta_o) \int_{L_m(z',\cos\theta_o)}^\infty dL \frac{dN_{S'}(z', L, \cos\theta_o)}{dL d(\cos\theta_o)}, \quad (5)$$

where $L_m(z, \cos\theta_o)$ is the minimum detectable luminosity of an SGRB with inclination angle θ_o and redshift z. The local rate density of SGRBs in Equation (4) can be estimated by comparing the predicted theoretical value of N(z) in Equation (5) to observations.

Throughout this paper we consider a standard flat, vacuum-dominated cosmology (Spergel et al. 2007). The expression for the comoving shell in Equation (5) takes the form

$$\frac{dV(z)}{dz} = 4\pi \left(\frac{c}{H_0}\right)^3 I(z)^2 \frac{dI(z)}{dz},\tag{6}$$

where

$$I(z) = \int_0^z \frac{dz'}{\sqrt{\Omega_M (1+z')^3 + \Omega_\Lambda}},\tag{7}$$

 $c=299,792.458~{\rm km\,s^{-1}}$ is the speed of light in vacuum, $H_0=67.8(9)~{\rm km\,s^{-1}\,Mpc^{-1}}$ is the Hubble constant, and $\Omega_M=0.308\pm0.012$ and $\Omega_\Lambda=0.692\pm0.012$ are the present ratio of matter and dark energy density in the universe relative to the critical density, respectively (Patrignani et al. 2016). Uncertainties in the above parameters affect our final results by less than 1% and can be safely neglected.

Since we consider an axially symmetric structured jet emission, the SGRB absolute luminosity is related to the SGRB luminosity distance

$$d_L(z) = (1+z)\frac{c}{H_0} \int_0^z dz' \left[\Omega_M (1+z')^3 + \Omega_\Lambda\right]^{-1/2}, \quad (8)$$

and to the SGRB isotropic equivalent luminosity L_I , i.e., the luminosity that the SGRB would have if it emitted isotropically as in the direction of the observer by

$$L = L_I \int_0^1 d(\cos \theta) \frac{l(\theta)}{l(\theta_o)}, \quad L_I = 4\pi d_L^2 k(z) F_o, \tag{9}$$

where $l(\theta)$ is the luminosity profile, F_o is the measured time-averaged energy flux in the detector's energy band and k(z) is the cosmological k-correction factor. Under the assumption that the SGRB spectral shape is independent from the inclination angle, F_o can be expressed as

$$F_o = \int_{e_1}^{e_2} Ef_o(E) dE = \frac{1}{(1+z)^2} \int_{e_1(1+z)}^{e_2(1+z)} Ef_s(E) dE, \quad (10)$$

where e_1 and e_2 denote the lower and upper cutoff values of the detector's observational energy range, and f_o and f_s are the photon flux density in the observer and source frame, respectively. The cosmological k-correction accounts for the unobserved fraction of the source spectrum. It is given by (Bloom et al. 2001)

$$k = \int_{E_1}^{E_2} Ef_s(E) dE / \int_{e_1(1+z)}^{e_2(1+z)} Ef_s(E) dE,$$
 (11)

where E_1 and E_2 are the lower and upper energy values of the SGRB spectrum. We use typical values $E_1=1~\rm keV$ and $E_2=10~\rm MeV$ and the phenomenological "Band function" (Band et al. 1993) with typical values of low- and high-energy indices $\alpha=-1$ and $\beta=-2.5$ for the source-frame photon flux density (Lien et al. 2016). We use the source-frame peak energy $E_{\rm peak}^s=800~\rm keV$ as suggested by Wanderman & Piran (2015). With this choice, the relative differences of the time-averaged energy flux and photon flux calculated with the power-law function and the Band function for the SGRB sample are on average $\sim\!23\%$ and $\sim\!11\%$, respectively, when the photon flux density of the two functions are normalized at 50 keV (Lien et al. 2016).

The number of SGRBs in Equation (5) depends on the metallicity of the SGRB progenitor, which is a function of the redshift (Belczynski et al. 2010, 2011). However, for small values of z the uncertainty due to this effect is expected to be subdominant w.r.t. uncertainties arising from other factors, such as the RF. Therefore, we will safely neglect the z

dependence on $N_{S'}$. In addition, we assume the number of SGRBs to be uniformly distributed in $\cos \theta_o$. With these assumptions, we can define the LF $\Phi(L)$ as

$$\frac{dN_{S'}}{dL}\Big|_{z=0} = \Phi(L)\cos\theta_o. \tag{12}$$

An SGRB can be detected if $F_o \ge F_m$, where F_m is the minimum EM flux that can be measured in the detector's energy band. We consider the NGSO-BAT fiducial 5σ energy flux threshold $F_m = 2.8 \times 10^{-8} \, \mathrm{erg \, s^{-1} \, cm^{-2}}$ with a duration of 1 s (Myers 2017). 96% of NGSO-BAT SGRBs have the time-averaged flux above this threshold, where the time-averaged energy flux is calculated with the best-fit spectrum model (Lien et al. 2016).

The detector introduces a bias in the determination of the LF. As the instrument has a minimum detection threshold, the larger the SGRB distance the fewer low-luminosity SGRBs are observed w.r.t. actual distribution. Thus the fit against observational data underestimates the number of fainter SGRBs. The observed LF is obtained by rescaling the LF by the volume where the detector is sensitive (Petrillo et al. 2012):

$$\Phi_o(L) = (d_{\star}/d_M)^{-3}\Phi,$$
 (13)

where d_{\star} is an arbitrary distance scale and

$$d_M \propto \sqrt{L}$$
 (14)

is the maximum distance at which an SGRB of luminosity L can be observed by the detector, where we have marginalized on the redshift and inclination angle. The luminosity profile of a structured jet profile with uniform emission in a cone of aperture $2\theta_c$ and power-law decay at larger angles is (Pescalli et al. 2015)

$$l(\theta) = \begin{cases} 1 & \text{for } \cos \theta_c \leqslant |\cos \theta| \leqslant 1, \\ \left(\frac{\theta}{\theta_c}\right)^{-s} & \text{for } 0 \leqslant |\cos \theta| < \cos \theta_c, \end{cases}$$
 (15)

where s>0 and θ_c are constant parameters and s, θ_c are identical for all SGRBs. Throughout the paper we will refer to the emission in the region $\cos\theta_c\leqslant|\cos\theta|\leqslant1$ as on-axis emission. As the LF is not known, we consider two different phenomenological functions (Andreon et al. 2006; Guetta & Piran 2006). The Schechter LF is

$$\Phi_o(L) = \Phi_{\star} \left(\frac{L}{L_0}\right)^{-\alpha} e^{-L/L_0} \text{ for } L \geqslant \frac{L_0}{\Delta}, \tag{16}$$

where Φ_{\star} , L_0 , α , and Δ are constant positive parameters. Δ determines the low-luminosity cutoff of the LF. The broken power LF is

$$\Phi_o(L) = \Phi_{\star} \begin{cases} \left(\frac{L}{L_0}\right)^{-\alpha} & \text{for } \frac{L_0}{\Delta_1} \leqslant L < L_0, \\ \left(\frac{L}{L_0}\right)^{-\beta} & \text{for } L_0 \leqslant L < \Delta_2 L_0, \end{cases}$$
(17)

where Φ_{\star} , L_0 , α , β , Δ_1 , and Δ_2 are constant positive parameters. Δ_1 and Δ_2 define the low- and high-luminosity cutoffs of the LF, respectively. If all SGRBs in a given sample

have the same inclination angle, for example, they are all seen on-axis, L can be replaced with L_I in Equations (16) and (17).

The SGRB RF is expected to follow the star RF, $R_{\star}(z)$. However, the delay between the time of star formation and the time of the binary system coalescence affects the form of the RF. This delay time depends, among other factors, on the initial separation of the stars and the orbital eccentricity of the binary system. Therefore, the SGRB RF is given by the convolution of the star RF with the distribution of the delay time, P(t) (Wanderman & Piran 2015). Observations of binary neutron star systems (Champion et al. 2004) indicate that P(t) is proportional to 1/t with $t \gtrsim 20$ Myr (Guetta & Piran 2006). Studies with StarTrack population synthesis software (Dominik et al. 2012) suggest a delay of \sim 20 (100) Myr for NSNS (NSBH) mergers. Champion et al. (2004) consider a typical delay time of the order of 1 Gyr. The retarded SGRB RF is

$$R_S(z) = \int_{t_m}^{T(\infty) - T(z)} dt \, \frac{1}{1 + z_*} R_*(z_*) P(t), \tag{18}$$

where the factor $(1 + z_{\star})^{-1}$ accounts for the difference between the star formation time and the coalescence time, t_m is the minimum delay time, and $z_{\star} = Z[T(z) + t]$ is the redshift when the progenitors form. The *look-back time* T(z) and its inverse Z(t) are (Hogg 1999)

$$T(z) = \frac{1}{H_0} \int_0^z \frac{dz'}{(1+z')\sqrt{\Omega_M(1+z')^3 + \Omega_\Lambda}},$$
 (19)

$$Z(t) = \left(\frac{\Omega_{\Lambda}}{\Omega_{M}}\right)^{1/3} \left[\left(\frac{1 + E(t)}{1 - E(t)}\right)^{2} - 1 \right]^{1/3} - 1, \tag{20}$$

where

$$E(t) = \exp\left[\ln\left(\frac{1+\sqrt{\Omega_{\Lambda}}}{1-\sqrt{\Omega_{\Lambda}}}\right) - 3H_0\sqrt{\Omega_{\Lambda}}t\right]. \tag{21}$$

The star RF can be estimated through semianalytical or numerical simulation methods. Both approaches require a number of assumptions on dust obscuration corrections and the stellar initial mass function (Wilkins et al. 2008). As a result, different models may predict quite different RFs. In the following, we define $R_{\star} = \tilde{R}_{\star} (c/H_0)^{-3}$ and consider six different star formation models:

 CHW (Cole et al. 2001; Hopkins & Beacom 2006; Wilkins et al. 2008):

$$\tilde{R}_{\star}(z) = R_0 \frac{a + bz}{1 + (z/c)^d} H(z),$$

$$H(z) = H_0 \sqrt{(1+z)^3 \Omega_{\rm M} + \Omega_{\Lambda}},$$
(22)

where a = 0.0166, b = 0.1848, c = 1.9474, d = 2.6316 for the Cole model, a = 0.0170, b = 0.13, c = 3.3, d = 5.3 for the Hopkins model, and a = 0.014, b = 0.11, c = 1.4, d = 2.2 for the Wilkins model, respectively.

2. Fardal (Fardal et al. 2007):

$$\tilde{R}_{\star}(z) = R_0 \frac{(1+z)^{p_2}}{[1+p_1(1+z)^{p_2}]^{p_3+1}} H(z), \tag{23}$$

where $p_1 = 0.075$, $p_2 = 3.7$, and $p_3 = 0.84$.

Table 1
Best-fit Parameters for the Schechter and Broken Power LFs

	p_1	p_2	<i>p</i> ₃	p_4
Schechter	51.6 ± 0.2	0.55 ± 0.07		3.2 ± 0.2
Broken power	51.5 ± 0.1	0.60 ± 0.05	2.4 ± 0.3	3.0 ± 0.3

Note. The parameters are $(p_1, p_2, p_4) = (\log_{10} L_0, \alpha, \log_{10} \Delta)$ for the Schechter LF and $(p_1, p_2, p_3, p_4) = (\log_{10} L_0, \alpha, \beta, \log_{10} \Delta_1)$ for the broken power LF. The values in the table are obtained by averaging on the parameters of each curve shown in Figure 2. Uncertainties are standard deviations.

3. Porciani (Porciani & Madau 2001):

$$\tilde{R}_{\star}(z) = R_0 \frac{e^{3.4z}}{e^{3.4z} + 22}.$$
(24)

4. Hernquist (Hernquist & Springel 2003):

$$\tilde{R}_{\star}(z) = R_0 \frac{\chi^2}{1 + \alpha(\chi - 1)^3 e^{\beta \chi^{7/4}}}, \quad \chi(z) = \left[\frac{H(z)}{H_0}\right]^{2/3},$$
(25)

where $\alpha = 0.012$, $\beta = 0.041$.

The normalization constants R_0 in the previous equations are chosen so that $R_s(0) = 1$. The RFs are shown in Figure 1.

3. LF and Jet Geometry

Table 4 in Appendix A lists the SGRBs used in our analysis. Following Fong et al. (2017), we assume that all SGRBs in the sample were observed on-axis. We evaluate the parameters of the LF with the exception of Δ_2 in Equation (17) by fitting Equations (16) and (17) against the cumulative number of SGRBs in our sample. The value of Δ_2 does not significantly affect the determination of the other parameters provided that $\Delta_2 \gg 1$. Guetta & Piran (2006) choose $\Delta_2 = 10^2$. For the sake of computational efficiency, we set $\Delta_2 = 10^3$. The best fits of the LF models are shown in Figure 2 for different choices of bin widths. The best-fit parameters are summarized in Table 1.

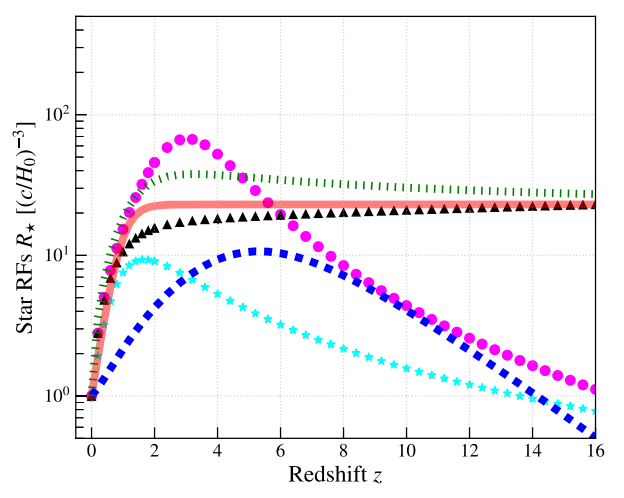
Using the LF and GW170817/GRB 170817A observational data, we can constrain the SGRB flux parameters θ_c and s. Assuming that GRB 170817A is seen off-axis, its (measured) isotropic equivalent luminosity must be rescaled to compare it to the isotropic equivalent luminosity of the SGRBs in the NGSO-BAT sample (which are seen on-axis). Using Equation (15) in Equation (9) the absolute luminosity of an SGRB in the NGSO-BAT sample can be written as

$$L = L_I \eta(\theta_c, s), \quad \eta = 1 - \cos \theta_c + \int_0^{\cos \theta_c} d(\cos \theta) \left(\frac{\theta}{\theta_c}\right)^{-s}.$$
(26)

The absolute luminosity \mathcal{L} of GRB 170817A can be written as

$$\mathcal{L} = \mathcal{L}_I \eta \left(\frac{\theta_G}{\theta_c} \right)^s, \tag{27}$$

where \mathcal{L}_I and θ_G are the isotropic equivalent luminosity and inclination angle of GRB 170817A, respectively. If we assume that GRB 170817A is a typical SGRB, we can substitute $\mathcal{L} = \langle L_I \rangle \eta$ in Equation (27), where $\langle L_I \rangle$ is the typical SGRB



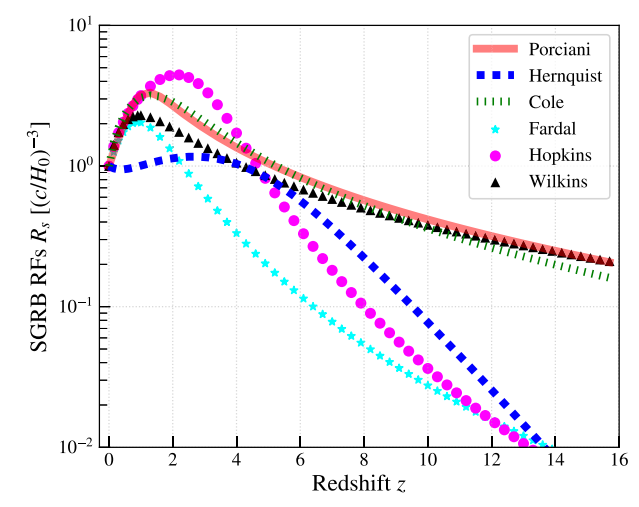


Figure 1. Star RFs R_{\star} (left panel) and SGRB RFs R_{S} with minimum delay time $t_{m}=20$ Myr (right panel) in units of $(c/H_{0})^{-3}$. The solid, dashed, dotted, square-marked, circle-marked, and triangle-marked curves denote the Porciani, Hernquist, Cole, Fardal, Hopkins, and Wilkins RFs, respectively. The RFs in the left panel are normalized to $R_{\star}(0)=1$ for the sake of comparison. The RFs in the right panel are normalized to $R_{S}(0)=1$.

luminosity. Solving for s, we find

$$s = \frac{\ln[\langle L_I \rangle / \mathcal{L}_I]}{\ln[\theta_G / \theta_c]}.$$
 (28)

Equation (28) allows us to set constraints on the (θ_c, s) parameter space. We estimate $\mathcal{L}_I = 2.3 \times 10^{47} \, \mathrm{erg \, s^{-1}}$ by converting the time-average flux observed by Fermi-GBM without soft-tail emission, $\mathcal{F}_{GBM} \sim 3.1 \times 10^{-7} \, \mathrm{erg \, s^{-1} \, cm^{-2}}$, to the flux in NGSO-BAT's spectrum range, $\mathcal{F}_{NGSO} \sim 1.5 \times$ $10^{-7}\,\mathrm{erg}\,\mathrm{s}^{-1}\,\mathrm{cm}^{-2}$ and using GW observational data for the inclination angle and the luminosity distance $d_{\mathcal{L}} = 40$ Mpc (Abbott et al. 2017a). The estimate of the inclination angle depends on several assumptions, most notably the spins of the neutron stars. VLBI observations suggest an inclination angle of $20^{\circ} \pm 5^{\circ}$ (Mooley et al. 2018). In the following we will conservatively consider a larger range of values $\theta_G = 15^{\circ}-40^{\circ}$, which is consistent with the 90% c.l. interval given in Abbott et al. (2019). The typical SGRB isotropic equivalent luminosity $\langle L_I \rangle$ is estimated by calculating the median of each LF best fit in Figure 2 and then averaging over the values. Figure 3 shows two examples of flux profiles compatible with Equation (28).

The assumption that GRB 170817A is seen off-axis implies $\theta_c < \theta_G$. The LIGO network observed one NSNS merger in the second observation run (O2). The probability densities P_c and P_s for θ_c and s can be expressed in terms of the truncated Poisson distribution

$$P_{\{c,s\}}(x) = \frac{\lambda(x)e^{-\lambda(x)} \left| \frac{d\lambda}{dx} \right|}{\int_0^a dx \ \lambda(x)e^{-\lambda(x)} \left| \frac{d\lambda}{dx} \right|},\tag{29}$$

where $a=\theta_G$ ($a=\infty$) for $x=\theta_c$ (x=s) and $\lambda=\mathcal{R}\rho_G\mathcal{V}_{LH}T_G$ is the expected number of NSNS mergers detected in the O2 search volume \mathcal{V}_{LH} and observing time T_G ,

$$\rho_G = \rho_S / [\Gamma_{\text{NSNS}} \mathcal{R} + \Gamma_{\text{NSBH}} (1 - \mathcal{R})]$$
 (30)

is the local rate density of the sum of NSNS and NSBH mergers, where $\mathcal R$ is the fraction of NSNS mergers to the total number of NSNS+NSBH mergers, $\Gamma_{\rm NSNS}$ and $\Gamma_{\rm NSBH}$ are the

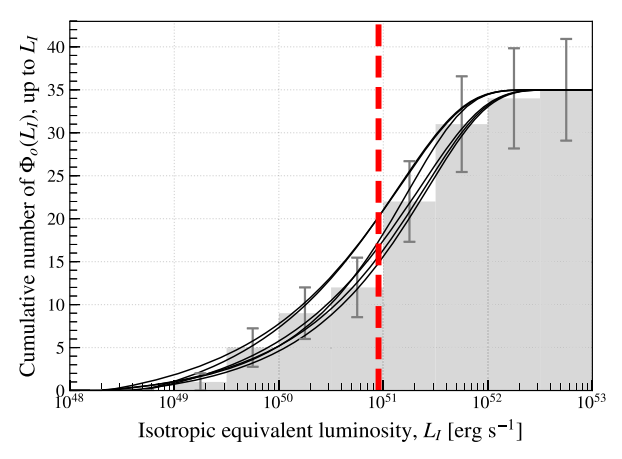
fraction of NSNS and NSBH mergers that produce SGRBs, respectively. The effective range for NSNS mergers in O2 was $V_{\rm LH}=88$ Mpc with an effective observation time of $T_G\sim 0.3$ yr.

Abbott et al. (2017a) estimate the rate of local NSNS mergers to be between 340 and 4740 Gpc⁻³ yr⁻¹. The NSBH rate is highly uncertain, but null detection in the LIGO first observation run (O1) gives an upper bound of $\sim 3600 \, {\rm Gpc}^{-3} \, {\rm yr}^{-1}$ (Abbott et al. 2016). We consider a range for \mathcal{R} from $\mathcal{R} = 0.5$, corresponding to an NSBH merger rate compatible with the NSNS merger rate, to $\mathcal{R}=1$, corresponding to an NSBH merger rate equal to zero. We set $\Gamma_{\rm NSNS}=1$ and consider $\Gamma_{\rm NSBH}$ in the the range 0.1–0.3 (Stone et al. 2013). We estimate the local rate density ρ_G for each different LF, RF, t_m , and jet parameters and then average over the LF best fits. We use NGSO's observation time of 12.6 yr with a duty cycle factor of 78%, corresponding to $T_o = 9.8 \text{ yr}$ (Lien et al. 2016) and averaged BAT's field of view of 1.4 sr (Barthelmy et al. 2005), corresponding to $f_{FOV} = 0.1$. 107 SGRBs were observed during 12.6 yr, leading to $f_r = 35/107$ (Lien et al. 2016). As the various RFs are comparable for $z \leq 1$ (see Figure 1), the choice of RF does not significantly affect the overall result. Therefore, for the sake of illustration, we only present the results for the Hernquist and Hopkins RFs with $t_m = 100 \,\mathrm{Myr}$ and 20 Myr, respectively.

Larger values of \mathcal{R} lead to a larger expected number of NSNS mergers in O2. Greater values of ρ_G imply a smaller half aperture angle to match the observed SGRB population. For instance, the value of θ_c calculated with $\mathcal{R}=1$ is 10% greater than the value calculated with $\mathcal{R}=0.5$. Similarly, larger values of $\Gamma_{\rm NSBH}$ imply a lower number of NSNS mergers in O2. A value of θ_c obtained with $\Gamma_{\rm NSBH}=0.1$ is 3% larger than the value obtained with $\Gamma_{\rm NSBH}=0.3$.

In the following, we choose as representative values $\Gamma_{\text{NSBH}}=0.2$ and $\mathcal{R}=5/6$, the latter corresponding to the ratio of the median value of the local rate density of NSNS mergers from Abbott et al. (2017a) and the median value of the local rate density of NSBH mergers from Abbott et al. (2016).

Figure 4 shows the jet parameter probability densities for different values of the GRB 170817A inclination angle. The color scale denotes the probability density of the GRB 170817A inclination angle for the "PhenomPNRT" waveform



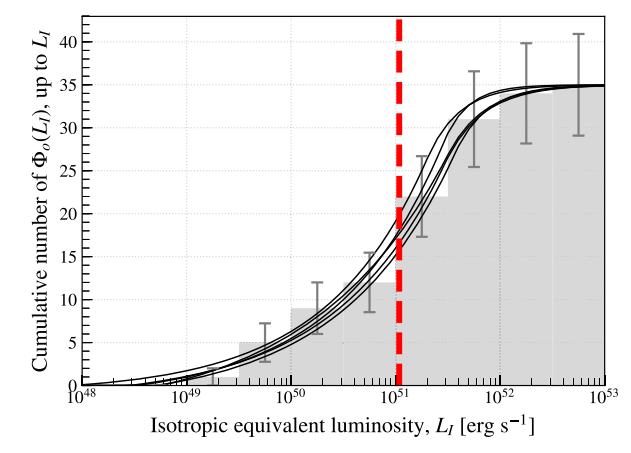


Figure 2. Best fits for the Schechter (left) and broken power (right) cumulative LFs, $\Phi_o(L_I)$. The curves denote least-square best fits with widths passing a chi-square two-tailed test at a 90% confidence level for different widths of the histogram bins in log scale, $\Delta l \equiv \log_{10}(L_n/L_{n-1})$, where $\Delta l \in [0.1, 1.0]$ and n is the bin index. Error bars in the histograms denote statistical uncertainties. The red dashed vertical lines give the average of the medians calculated for each LF best fit.

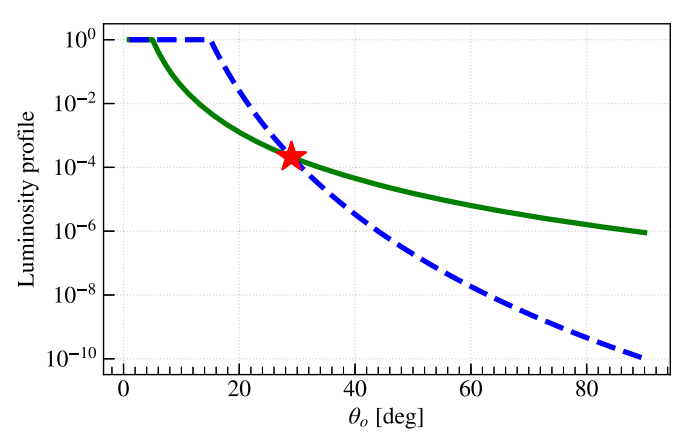


Figure 3. Luminosity profile of GRB 170817A as a function of the inclination angle for two choices of the jet parameters. The solid green and dashed blue curves give the luminosity profile for $(\theta_c, s) = (5^\circ, 4.8)$ and $(\theta_c, s) = (15^\circ, 12.8)$, respectively. The star denotes the isotropic equivalent luminosity of GRB 170817A normalized to the typical SGRB isotropic equivalent luminosity for an inclination angle of $\theta_G = 29^\circ$, corresponding to the median value of the probability density from Abbott et al. (2019).

model with low-spin prior (see Figure 4 in Abbott et al. 2019). The most likely values of θ_c are comparable throughout any values of inclination angle θ_G . However, the values of s are smaller for larger values of θ_G . Hence, a larger θ_G increases the chance of detecting off-axis SGRBs relative to on-axis SGRBs.

Figure 5 shows the allowed region of the (θ_c, s) parameter space. The colored region bounded by the solid and dashed blue curves represents the allowed region for the 90% and 50% c.l. intervals of the observed GRB 170817A inclination angle, respectively. The color scale represents the probability of having a given opening angle θ_c with the solid and dashed cyan curves denoting 90% and 50% c.l. intervals. Table 2 shows values of θ_c and s for different LFs, RFs, t_m and $\theta_G = 29^\circ$, which corresponds to the median value of the probability density of the inclination angle in Abbott et al. (2019).

4. Local Rate Density and Number of Coincident Events

Using the values of θ_c from Table 2 we can estimate the local rate density of GW events and the projected number of

observations by a network of GW detectors. The local rate density varies between $\rho_G=1100\pm1000\,\mathrm{Gpc^{-3}\,yr^{-1}}$ and $\rho_G=4500\pm4300\,\mathrm{Gpc^{-3}\,yr^{-1}}$, where the lower (upper) value is obtained from the 1σ larger (smaller) value of θ_c in Table 2 and the uncertainties follow from the 1σ uncertainties from averaging over the LF best fits. The median value of θ_c for the various models gives $\rho_G=2400\,\mathrm{Gpc^{-3}\,yr^{-1}}$, which can be considered as the best estimate for the local rate density. The uncertainty in the local rate density is mainly due to the uncertainty in the determination of the jet opening angle. Smaller values of θ_c imply fewer observable SGRBs and a larger number of actual binary system coalescences to match observations. For instance, $\theta_c=7^\circ$ for the model with the Hopkins RF, the broken power LF and 20 Myr delay time leads to a local rate density that is \sim 4 times larger than the local rate density calculated with $\theta_c=16^\circ$.

To see how the various RFs, LFs, and delay times affect the local rate density estimate, we arbitrarily fix the jet opening angle to $\theta_c = 10^{\circ}$ and vary all other parameters (see Figure 6). The Hopkins RF is characterized by a higher SGRB formation rate at small z w.r.t. other RFs (see the right panel of Figure 1), thus implying a lower local rate density to fit observations. The Hernquist RF typically gives local rate densities about 1.8 times larger than the local rate densities obtained with the Hopkins RF (see right panel of Figure 1). Shorter minimum delay times imply smaller initial orbital separations of the compact objects and a faster evolution of the binary system toward coalescence. As the number of SGRBs tends to peak at larger z, shorter minimum delay times lead to smaller local rate densities. A minimum delay time $t_m = 20 \,\mathrm{Myr}$ gives a local rate density approximately 90% smaller than the local rate density obtained with $t_m = 100 \,\mathrm{Myr}$. The broken power LF leads to local rate densities 29% larger than the local rate densities obtained with the Schechter LF. The broken power LF predicts a larger population of intrinsically faint SGRBs than the Schechter LF, suggesting the existence of a larger population of faint distant SGRBs that may escape detection. For example, the minimum cutoff luminosity of the broken power LF obtained by averaging the LF best fits in Figure 2 is $\sim 1\%$ smaller than the minimum cutoff luminosity of the Schechter LF.

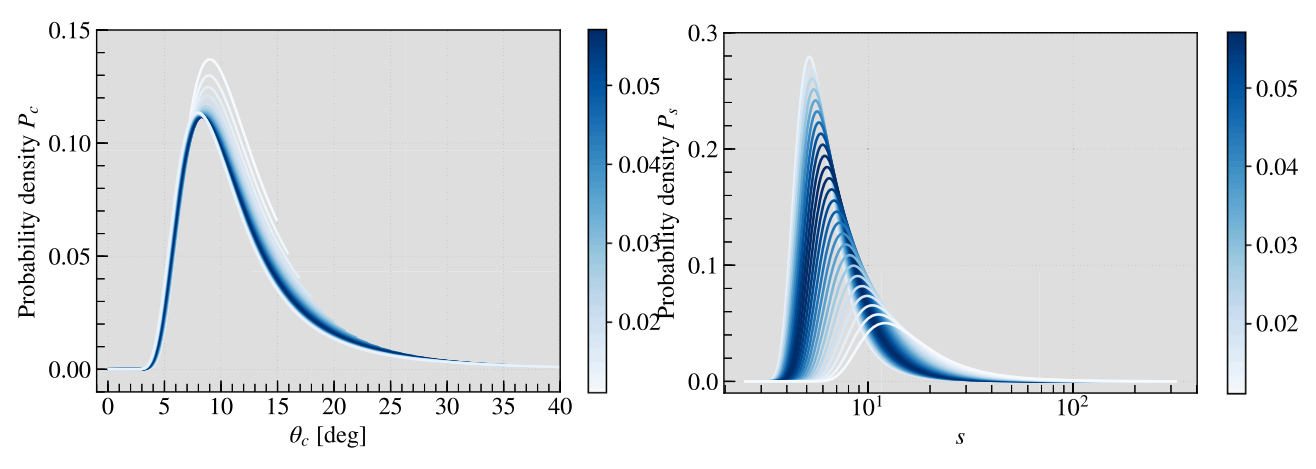


Figure 4. Probability densities of the jet parameters P_c (left panel) and P_s (right panel) for the broken power LF, the Hopkins RF and delay time $t_m = 20$ Myr and different values of $\theta_G \in [15^\circ, 40^\circ]$. The probability densities are obtained by averaging over the LF best fits of Figure 2. The color scale indicates the probability density of the observed GRB 170817A inclination angle from Abbott et al. (2019).

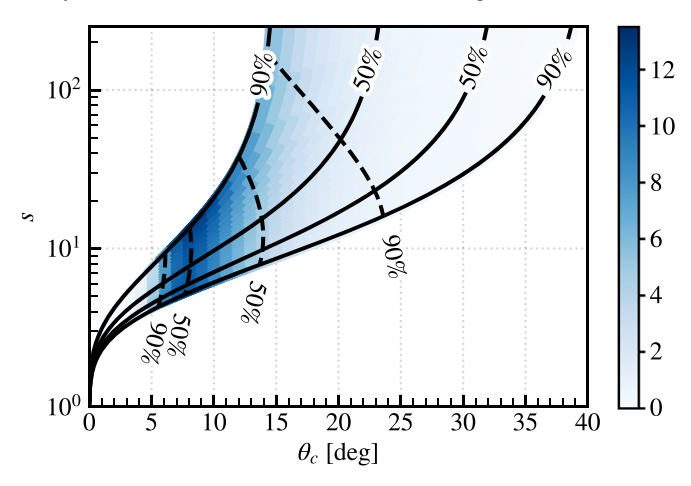


Figure 5. Allowed region of the jet parameter space. The colored region bounded by the solid black curves represents the allowed regions of the jet parameter space obtained by considering the 90% and 50% c.l. intervals for the observed GRB 170817A inclination angle (Abbott et al. 2019). The values of θ_G increase from left to right. The color scale represents the probability for the opening angle θ_c . The dashed black curves give the lower and upper bounds at 90% and 50% c.l.

Table 2
Best Estimates of the Jet Parameters for Different LFs, RFs, and Minimum Delay Times

LF	RF	t _m (Myr)	θ_c (deg)	S
	Id	i _m (iviyi)		
Schechter	Hernquist	100	$13.0^{+6.8}_{-4.0}$	$10.3^{+11.5}_{-3.2}$
		20	$12.9^{+6.8}_{-4.0}$	$10.3^{+11.3}_{-3.2}$
	Hopkins	100	$9.5^{+5.6}_{-3.0}$	$7.4^{+5.3}_{-1.9}$
		20	$9.0_{-2.8}^{+5.3}$	$7.1^{+4.7}_{-1.7}$
Broken power	Hernquist	100	14.8+6.9	$12.6^{+16.8}_{-4.4}$
		20	$14.8^{+6.9}_{-4.5}$	$12.5_{-4.3}^{+16.6}$
	Hopkins	100	$11.0^{+6.2}_{-3.4}$	$8.7^{+7.4}_{-2.4}$
		20	$10.3^{+5.9}_{-3.2}$	$8.2^{+6.5}_{-2.2}$

Note. The Values in the table are the median values of the P_c and P_s distributions calculated with $\theta_G = 29^{\circ}$. Quoted uncertainties are at 68% c.l.

Given the local rate density, we can estimate the number of GW events and the number of coincident GW-SGRB events observable by a network of GW detectors and EM partners. Let us define the duty cycle factor of a network comprising $\mathcal{N}\geqslant 2$

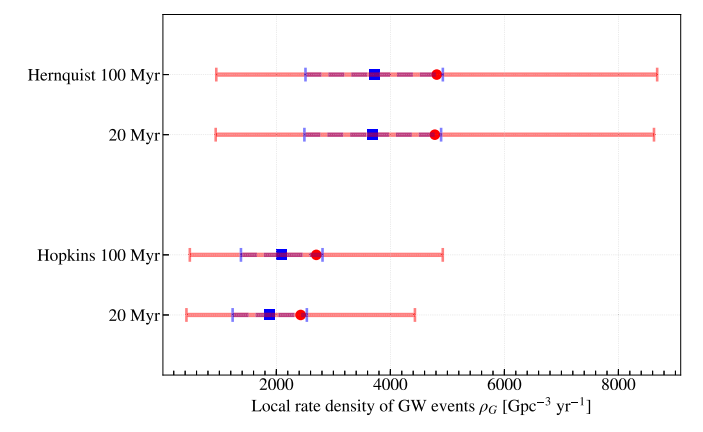


Figure 6. Local rate density calculated for different RFs, minimum delay times and LFs (red = broken power, blue = Schechter) with a fixed jet opening angle $\theta_c = 10^\circ$ and $\theta_G = 29^\circ$. The red circles and blue squares denote the average values of ρ_G for the broken power and the Schechter LFs, respectively. The bars designate 1σ uncertainties due to the LFs. The Hernquist RF and the Schechter LF give local rate densities typically higher than the Hopkins RF and the broken power LF.

GW detectors as

$$\mathcal{D}_{i_1 \cdots i_N} \equiv \prod_{k=1}^{N} [D_k^{i_k} (1 - D_k)^{1 - i_k}], \tag{31}$$

where $k=1,\cdots,\mathcal{N}$ is a label uniquely identifying the detectors, D_k is the duty cycle factor of the kth detector, and $i_k=(0,1)$ indicates whether the kth detector is in observing mode $(i_k=1)$ or not in observing mode $(i_k=0)$. (See Appendix B for a derivation of Equation (31) and following equations.) For example, in the case of the Advanced LIGO network comprising the LIGO-Livingston (LLO) detector with duty cycle factor D_1 and the LIGO-Hanford (LHO) detector with duty cycle factor D_2 , the network duty cycle factor is

$$\mathcal{D}_{i_1 i_2} \\ = \begin{cases} D_1 D_2 & \text{LLO observing and LHO not observing,} \\ D_1 (1 - D_2) & \text{LLO observing and LHO not observing,} \\ (1 - D_1) D_2 & \text{LLO not observing and LHO observing,} \\ (1 - D_1) (1 - D_2) & \text{LLO and LHO not observing.} \end{cases}$$

(32)

The fraction of time a given subset of m detectors are in observing mode is given by Equation (31) with $i_k = 1$ for $k \in \{m\}$ and $i_k = 0$ for $k \notin \{m\}$. Using Equation (31), the total number of NSNS and NSBH mergers that can be simultaneously observed by at least two detectors in the network is

$$N_G = \rho_G T_G \sum_{i_1=0}^{1} \cdots \sum_{i_{\mathcal{N}}=0}^{1} \mathcal{D}_{i_1 \cdots i_{\mathcal{N}}} [\mathcal{R} \mathcal{V}_{i_1 \cdots i_{\mathcal{N}}} + (1 - \mathcal{R}) \mathcal{U}_{i_1 \cdots i_{\mathcal{N}}}],$$
(33)

where T_G is the network running time and $\mathcal{V}_{i_1\cdots i_N}$ ($\mathcal{U}_{i_1\cdots i_N}$) is the second largest single-detector NSNS (NSBH) search volume when at least two detectors are in observing mode (zero otherwise). Similarly, the number of mergers that are observable by at least two GW detectors in coincidence with an EM detector is

$$N_{C} = \frac{T_{G}D_{\text{EM}}f_{\text{EM}}}{fT_{o}} \sum_{i_{1}=0}^{1} \cdots \sum_{i_{\mathcal{N}}=0}^{1} \mathcal{D}_{i_{1}\cdots i_{\mathcal{N}}}[\mathcal{P}N(\mathcal{Z}_{i_{1}\cdots i_{\mathcal{N}}}) + (1-\mathcal{P})N(\mathcal{Y}_{i_{1}\cdots i_{\mathcal{N}}})],$$
(34)

where

$$\mathcal{P} = \frac{\Gamma_{\text{NSNS}} \mathcal{R}}{\Gamma_{\text{NSNS}} \mathcal{R} + \Gamma_{\text{NSBH}} (1 - \mathcal{R})}$$
(35)

is the fraction of SGRBs that are produced by NSNS mergers, $D_{\rm EM}$ is the duty cycle of the EM detector, $f_{\rm EM}$ is its field of view, and $N(\mathcal{Z}_{i_1\cdots i_{\mathcal{N}}})$ and $N(\mathcal{Y}_{i_1\cdots i_{\mathcal{N}}})$ are the numbers of SGRB from Equation (5) up to redshifts $\mathcal{Z}_{i_1\cdots i_{\mathcal{N}}}$ and $\mathcal{Y}_{i_1\cdots i_{\mathcal{N}}}$, corresponding to the search volumes $\mathcal{V}_{i_1\cdots i_{\mathcal{N}}}$ and $\mathcal{U}_{i_1\cdots i_{\mathcal{N}}}$, respectively. The total number of mergers that are observable by at least a single GW detector in coincidence with an EM detector can be obtained by setting $\mathcal{Z}_{i_1\cdots i_{\mathcal{N}}}$ and $\mathcal{Y}_{i_1\cdots i_{\mathcal{N}}}$ to the largest single-detector NSNS and NSBH detection redshifts, respectively.

To estimate the number of coincident events detectable between *Fermi*-GBM and a GW detector we set the field of view for *Fermi*-GBM to 70%, the duty cycle factor to 85% (Burns et al. 2016). Following Burns et al. (2016), we treat *Fermi*-GBM and NGSO-BAT as equally sensitive. To calculate the time-averaged energy flux threshold 1.0×10^{-7} erg cm⁻² s⁻¹ for *Fermi*-GBM in the energy band 10–1000 keV, we convert the fiducial energy flux threshold for NGSO-BAT from the observer-frame Band function, which is obtained using the source-frame Band function with the mean value z=0.69 from Wanderman & Piran (2015). About 94% of GBM SGRBs have the time-averaged flux above this threshold.

We assume conservative NSNS inspiral ranges of 120 Mpc for the LIGO detectors and 65 Mpc for Virgo in the third observing run (O3), and 190 Mpc for LIGO, 65 Mpc for Virgo, and 40 Mpc for KAGRA in the fourth observing run (O4) (Abbott et al. 2018). We also consider the scenario with NSNS inspiral ranges of 190 Mpc for LIGO, 125 Mpc for Virgo, and 140 Mpc for KAGRA at design sensitivity. We set the duty cycle factor of each detector to 80%. We assume the inspiral range for NSBH mergers to be approximately 1.6 times larger than the inspiral range of NSNS mergers (Abbott et al. 2018). The predicted rates of combined NSNS and NSBH mergers observable by at least two GW detectors in O3, O4 and at design sensitivity, and the corresponding predicted rates of coincident events observable by NGSO-BAT and Fermi-GBM are summarized in Table 3.

Table 3

Estimated Rates of Combined NSNS and NSBH GW Detections and Coincident EM Observations Per Calendar Year of Network's Observation Time by At Least Two GW Detectors or a Single GW Detector in O3, O4 and at the Detector Design Sensitivity

Obse	erving Run [Network]	O3[LHV]	O4[LHV]	Design [LHKV]
N_G/yr	two GW detectors	4–66	15–251	17–296
$N_C/{ m yr}$	NGSO-BAT (two GW detectors) Fermi-GBM (two GW detectors)	0.002-0.02 0.1-0.6	0.01–0.1 0.3–1.6	0.05–0.2 0.3–1.8
N_C/yr	NGSO-BAT (single GW detector) Fermi-GBM (single GW detector)	0.02–0.1 0.1–0.8	0.06–0.3	0.06–0.3

Note. The results are derived for the model with the broken power LF, Hopkins RF with delay time 20 Myr, and assuming a duty cycle factor of 80% for each GW detector. Ranges in the table are obtained by varying the jet half-opening angle in the 1σ interval [7.1, 16.2] (see Table 2) and the broken power LF best fits (See Figure 2). *L, H, V*, and *K* Stand for LIGO-Hanford, LIGO-Livingston, Virgo, and KAGRA, respectively. *Fermi*-GBM and NGSO-BAT teams are looking for subthreshold weak GRB signals that are missed with standard trigger criterion around the time when GW events are detected. Subthreshold detection could potentially increase N_C .

The rate of on-axis SGRB events can be obtained by replacing the lower bound of the $\cos \theta_0$ integral in Equation (5) with $\cos \theta_0$ multiplying by a factor of 2 and choosing f equal to the Fermi-GBM field of view. Figure 7 shows the rate of on-axis, off-axis, and total coincident events per calendar year detectable by Fermi-GBM and a single generic GW detector as a function of z. The fraction of off-axis detections for the LHV and the LHKV networks is estimated to be between 50% and 85% in O3, and 45% and 65% in O4 and at design sensitivity. As the NSBH search volume is greater than the NSNS search volume (by approximately a factor of 4), different choices of R and Γ_{NSBH} lead to different estimates on the number of coincident observations. Smaller values of \mathcal{R} imply a larger population of NSBH mergers and larger values of Γ_{NSBH} imply greater fractions of NSBH mergers producing SGRBs. For example, $\mathcal{R} = 0.5$ gives $N_C \sim 44\%$ larger than the value obtained with $\mathcal{R} = 1$ and $\Gamma_{\rm NSBH}=0.3$ gives $N_c\sim 9\%$ larger than the value obtained with $\Gamma_{\text{NSBH}} = 0.1$. The largest number of coincident events in O3, $N_C \sim 0.8$, is obtained with $\mathcal{R} = 0.5$ and $\Gamma_{\text{NSBH}} = 0.3$.

5. Discussion and Conclusion

Using a catalog of SGRB observations by NGSO-BAT (Gehrels et al. 2004) and EM and GW data from GW170817/GRB 170817A, we have estimated the local rate density of NSNS and NSBH coalescences and derived constraints on the geometry of SGRB jets. Our data sample comprises 35 SGRBs with known redshift that were observed by NGSO-BAT in an ~12 yr period, from 2004 December 17th to 2017 June 12th. We considered the Schechter and broken power models for the LF, and various models for the RF with different delay times.

We find that the typical value of the half-opening angle θ_c in a structured jet profile (Pescalli et al. 2015) is between 7° and 22° with the power-law decay exponent s varying between 5 and 30 at 1σ confidence level. Using these results, the local rate density of GW events across all considered models is

estimated to be between $\rho_G = 1100 \pm 1000 \, {\rm Gpc}^{-3} \, {\rm yr}^{-1}$ and $\rho_G = 4500 \pm 4300 \, {\rm Gpc}^{-3} \, {\rm yr}^{-1}$.

The choices of the LF and the RF affect these results. The broken power LF implies a larger population of low-luminous SGRBs. Thus models with the broken power LF lead to halfopening angles greater than those predicted by models with the Schechter LF. Narrower (wider) jet opening angles imply a larger (smaller) local rate density. For example, $\theta_c = 7^{\circ}$ leads to a local rate density \sim 4 times larger than the local rate density calculated with $\theta_c = 16^{\circ}$. The choice of RF is the factor that most affects the results. Different RFs lead to different estimates because of assumptions about the initial stellar mass functions, dust obscuration corrections, and minimum delay times. For example, the median value of the half-opening angle ranges from 9° for the Hopkins RF to 15° for the Hernquist RF. The model with the broken power LF, Hopkins RF, and the minimum delay time $t_m = 20 \,\mathrm{Myr}$ can be used as a representative example with most likely values $\theta_c = 10^{\circ}.3^{+5.9}_{-3.2}$ and $s = 8.2^{+6.5}_{-2.2}$. The rate of GW observations in O3 (O4) Advanced LIGO-Virgo observation run for this model is between $N_G \sim 4$ (17) and 66 (251) events per calendar year with a rate of coincident GW-SGRB observations by Fermi-GBM and at least two GW detectors in the network between $N_C \sim 0.1 \ (0.3)$ and 0.6 (1.6). About 50%–85% (45%–65%) of these events in O3 (O4) are expected to be detections of offaxis SGRBs. The corresponding values for the LIGO-Virgo-KAGRA network at design sensitivity are between $N_G \sim 17$ and 296, and $N_C \sim 0.3$ and 1.8 with a fraction of off-axis SGRBs comparable to O4. If only one GW detector is required to claim a coincident event, values increase by ~40% in O3 and O4 and by $\sim 20\%$ at network design sensitivity.

The composition of the SGRB sample may also affect the results. As a consistency check, we calculated the number of coincident GW-Fermi GBM observations in O3 without considering GRB 090417A and GRB 070923, whose localization is \sim 60 times worse than the localization of the other SGRBs in the sample. We found that the results did not significantly change ($N_C \sim 0.05$ –0.6) as their effect on the determination of the LF is minimal.

As a second consistency check, we also estimated the number of coincident observations by the two-detector LIGO network and Fermi-GBM in the latest O2 run and found $N_C \sim 0.02$ –0.1. In deriving this result, we assumed GRB 170817A to be a typical SGRB, i.e., we set the absolute luminosity of GRB 170817A equal to the median of the SGRB sample. If the actual absolute luminosity of GRB 170817A is lower, the jet profile must decay more slowly in order to match the observed luminosity. As the emission at wider angles provides the dominant contribution for detections at low z, the estimated upper bound of coincident GW-Fermi GBM observations could then increase. For example, by choosing the absolute luminosity of GRB 170817A one order of magnitude lower, we find $\theta_c = 9.8^{+6.9}_{-3.2}$, $s = 5.7^{+4.6}_{-1.5}$ and an estimated upper bound of coincident GW-Fermi GBM observations \sim 0.2. Different choices of $\mathcal R$ and Γ_{NSBH} can also lead to a larger N_C . If we set $\mathcal{R} = 0.5$ and $\Gamma_{\text{NSBH}} = 0.3$, the number of coincident GW-Fermi GBM observations in O2 can be as high as \sim 0.3 and between 0.2 (0.5) and 1.0 (2.0) for O3 (O4). KAGRA's contribution will be negligible, as its sensitivity in O4 is expected to be low enough to affect results only by a few percent \sim 1%. The above results are in agreement with the estimate of $N_C = 0.1-1.4$ events per year given in Abbott et al. (2017b), where an extended power-law LF with minimum isotropic

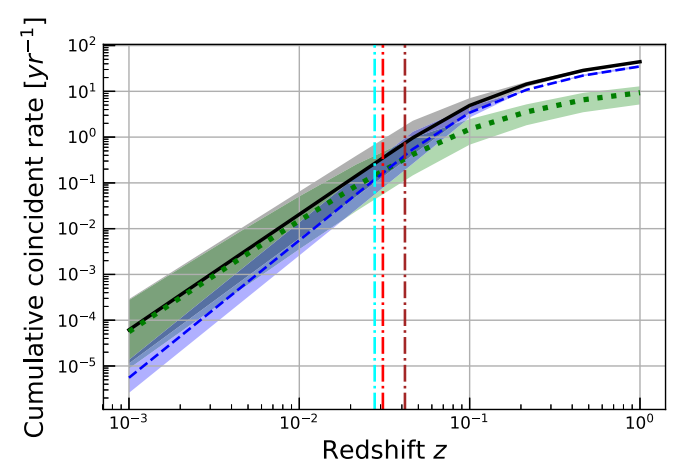


Figure 7. Rate of coincident events per calendar year detectable by *Fermi*-GBM and a single GW detector for the model with the Hopkins RF, minimum delay time 20 Myr, broken power LF, $\theta_c = 10^{\circ}3^{+5\,9}_{-3\,9}$ and $\theta_G = 29^{\circ}$ as a function of the redshift. The *Fermi*-GBM field of view and duty cycle factor are assumed to be 85% of the sky coverage and 70%, respectively. The duty cycle factor for the GW detector is 80%. The dashed blue curve denotes the rate of on-axis events, the dotted-green curve denotes the rate of off-axis events, and the solid black curve denotes the total rate. The dotted-dashed red, cyan, and gray curves represent the NSNS inspiral ranges for LIGO, Virgo and KAGRA at design sensitivity, respectively. The shaded areas denote 1σ uncertainties in the estimates due to θ_c and the LF best fits (see Figure 2).

luminosity of $10^{47} \, \mathrm{erg \, s^{-1}}$ is assumed to either account for off-axis dimmer events or the presence of a larger, low-luminosity population of SGRBs.

Recently, several other independent investigations have provided estimates for the expected rate of coincident GW and EM observations in future observing runs. Using Monte Carlo simulations with a structured jet model from Margutti et al. (2018), Gupte & Bartos (2018) estimate the percentage of coincident NSNS GW and Fermi-GBM observations to be about 30%. The larger number of coincident observations is mainly due to the assumption of a uniform inclination angle, which increases the chance of detecting on-axis emissions. Beniamini et al. (2019) consider several jet models, including a structured jet model, the Gaussian jet model, and a cocoon-like model to show that GRB 170817A is atypical. They estimate the number of coincident GW-Fermi GBM observations to be $\sim 1 \text{ yr}^{-1}$ within a distance of 220 Mpc. Bhattacharya et al. (2018) estimate the rates of coincident GW and EM detections (prompt and cocoon emission) to be in the range 0.8-4.4 yr⁻¹ at Advanced LIGO design sensitivity for a wide range of NSBH merger parameters such as mass, spin, and NS equation of state. Howell et al. (2018) perform a Bayesian inference using GRB 170817A EM data and the Gaussian jet model to predict coincident rates of 0.2–1.8 yr⁻¹ in O3 and 0.3-4 yr⁻¹ at design sensitivity. Both Fermi-GBM and NGSO-BAT teams are looking for subthreshold weak GRB signals that are missed with standard trigger criterion around the time when GW events are detected, which can potentially lead to additional coincident observations. No matter what nature decides to offer us, new coincident detections in upcoming observing runs will certainly allow us to refine these estimates and better constrain the geometry of the SGRB jets.

This work has been supported by NSF grants PHY-1921006 and PHY-1404139. The authors would like to thank colleagues at the LIGO Scientific Collaboration and the Virgo Collaboration for their help and useful comments. The authors are grateful for

computational resources provided by the LIGO Laboratory and supported by NSF grants PHY-0757058 and PHY-0823459. K. M. would like to thank all the LIGO Laboratory staff and LSC fellows for their support during his stay at LIGO Hanford Observatory, where part of this work was completed, and colleagues at the University of Mississippi, Shrobana Ghosh, Sumeet Kulkarni, and Dripta Bhattacharjee for their help.

Appendix A SGRB Data Sample

In our analysis, we consider the sample of SGRBs with known redshift from Myers (2018) and extend it to include SGRBs with redshift obtained through the observation of an afterglow, as shown in Siellez et al. (2017). The sample of the SGRBs is summarized in Table 4.

Table 4
List of the SGRBs Used in Our Analysis

List of the BORD's Osed in Our Analysis					
SGRB name	Flux $(10^{-7} \text{ erg cm}^{-2})$	Redshift	$L_{l}(\text{erg s}^{-1})$	Reference	
161104A	3.66	0.788	5.4×10^{51}	I	
160821B	2.15	0.16	1.1×10^{50}	II	
160624A	1.68	0.483	8.8×10^{50}	NGSO	
150423A	2.83	1.394	1.4×10^{52}	NGSO	
150120A	1.06	0.46	5.1×10^{50}	NGSO	
150101B	0.881	0.1343	3.2×10^{49}	III	
141212A	2.16	0.596	1.8×10^{51}	NGSO	
140903A	3.75	0.351	1.0×10^{51}	NGSO	
140622A	0.868	0.959	1.9×10^{51}	NGSO	
131004A	1.35	0.717	1.6×10^{51}	NGSO	
130603B	24.9	0.3565	6.9×10^{51}	IV	
120804A	8.82	1.3	3.7×10^{52}	V	
111117A	2.92	1.3	1.2×10^{52}	VI, VII	
101219A	3.86	0.718	4.7×10^{51}	NGSO	
100724A	1.03	1.288	4.2×10^{51}	NGSO	
100628A	5.27	0.102	1.1×10^{50}	VIII	
100625A	5.91	0.452	2.7×10^{51}	IX	
100206A	10.5	0.407	3.9×10^{51}	X	
100117A	2.89	0.915	5.8×10^{51}	XI	
090927	0.82	1.37	3.8×10^{51}	NGSO	
090515	4.65	0.403	1.7×10^{51}	XII	
090510	0.971	0.903	1.9×10^{51}	NGSO	
090426	1.35	2.609	2.2×10^{52}	NGSO	
090417A	1.75	0.088	2.7×10^{49}	XIII	
080905A	1.3	0.1218	3.8×10^{49}	XIIV	
070923	8.77	0.076	9.9×10^{49}	XV	
070729	0.9	0.8	1.4×10^{51}	XVI	
070724A	0.633	0.457	3.0×10^{50}	NGSO	
070429B	1.22	0.9023	2.4×10^{51}	XVII	
061217	1.67	0.827	2.7×10^{51}	NGSO	
061201	4.0	0.111	9.8×10^{49}	NGSO	
060801	1.47	1.1304	4.6×10^{51}	XVIII	
060502B	2.8	0.287	4.9×10^{50}	NGSO	
051221A	5.46	0.547	3.7×10^{51}	NGSO	
050509B	2.55	0.225	2.7×10^{50}	NGSO	

Note. Time-averaged energy flux is taken by Lien et al. (2016). L_I is the isotropic equivalent luminosity. The last column gives the reference for the redshift estimate: NGSO Data Center Archive (Myers 2018; NGSO); Fong & Chornock (2016; I); Levan et al. (2016; II); Fong et al. (2016; III); Postigo et al. (2014; IV); Berger (2013; V); Sakamoto (2013; VI); Margutti et al. (2012; VII); Nicuesa Guelbenzu et al. (2015; VIII); Fong et al. (2013; IX); Perley et al. (2012; X); Fong et al. (2011; XI); Berger (2010; XII); O'Brien & Tanvir (2009); Fox (2009); Bloom et al. (2009; XIII); Rowlinson et al. (2010; XIIV); Fox & Ofek (2007; XV); Leibler & Berger (2010; XVI); Cenko et al. (2008; XVII); Berger et al. (2007; XVIII).

Appendix B Network Duty Cycle Factor

In this appendix we derive Equations (31)–(34). Let us define \mathcal{R} as the fraction of NSNS mergers to the total number of NSNS and NSBH mergers, and T_G as the running time of a network comprising $\mathcal{N} \geqslant 2$ GW detectors. The fraction of the observation time of the kth detector is proportional to D_k or $(1-D_k)$ if the detector is observing or not, where D_k is the duty cycle factor of the kth detector and $k=1,...\mathcal{N}$ is a label uniquely identifying the detectors. The duty cycle factor of the network is given by Equation (31). By summing Equation (31) on all possible combinations of $i_k = (0, 1)$, where $i_k = 1$ (0) indicates that the kth detector is (not) in observing mode, we find

$$\sum_{i_{1}=0}^{1} \cdots \sum_{i_{N}=0}^{1} \mathcal{D}_{i_{1}\cdots i_{N}}$$

$$= \sum_{i_{1}=0}^{1} \cdots \sum_{i_{N}=0}^{1} \left\{ \prod_{k=1}^{N} \left[D_{k}^{i_{k}} (1 - D_{k})^{1-i_{k}} \right] \right\}$$

$$= \prod_{k=1}^{N} \left\{ \sum_{i_{k}=0}^{1} \left[D_{k}^{i_{k}} (1 - D_{k})^{1-i_{k}} \right] \right\}$$

$$= \prod_{k=1}^{N} \left[(1 - D_{k}) + D_{k} \right]$$

$$= 1, \tag{36}$$

as expected. The fraction of time a given subset of m detectors are in observing mode is given by Equation (31) with $i_k = 1$ for $k \in m$ and $i_k = 0$ for $k \notin m$:

$$T_{i_k \cdots i_N} = T_G \mathcal{D}_{i_k \cdots i_N}. \tag{37}$$

The number of observable events is given by the local rate density times the volume-time of the search. The combined number of NSNS and NSBH mergers is

$$N_{i_{1}\cdots i_{N}} = \{ [\rho_{G}\mathcal{R}]T_{i_{1}\cdots i_{N}}\mathcal{V}_{i_{1}\cdots i_{N}} \}$$

$$+ \{ [\rho_{G}(1-\mathcal{R})]T_{i_{1}\cdots i_{N}}\mathcal{U}_{i_{1}\cdots i_{N}} \},$$
(38)

where ρ_G is the combined local rate density of the NSNS and NSBH mergers, \mathcal{R} is the fraction of NSNS mergers to the total number of NSNS and NSBH mergers, $\mathcal{V}_{i_1\cdots i_N}$ ($\mathcal{U}_{i_1\cdots i_N}$) is the second largest single-detector NSNS (NSBH) search volume during the time $T_{i_1\cdots i_N}$ when two or more detectors are in observing mode (zero otherwise). By summing on all $i_k=(0,1)$ combinations, we find

$$N_{G} = \sum_{i_{1}=0}^{1} \cdots \sum_{i_{N}=0}^{1} N_{i_{1}\cdots i_{N}},$$

$$= \rho_{G} \sum_{i_{1}=0}^{1} \cdots \sum_{i_{N}=0}^{1} \{\mathcal{R}T_{i_{1}\cdots i_{N}}\mathcal{V}_{i_{1}\cdots i_{N}} + (1-\mathcal{R})T_{i_{1}\cdots i_{N}}\mathcal{U}_{i_{1}\cdots i_{N}}\}$$

$$= T_{G}\rho_{G} \sum_{i_{1}=0}^{1} \cdots \sum_{i_{N}=0}^{1} \{\mathcal{D}_{i_{1}\cdots i_{N}}[\mathcal{R}\mathcal{V}_{i_{1}\cdots i_{N}} + (1-\mathcal{R})\mathcal{U}_{i_{1}\cdots i_{N}}]\}.$$
(39)

As an example, we compute the number of NSNS mergers observable by the LHO and LLO network with duty cycles D_1 , D_2 and search volumes $V_1 \geqslant V_2$, respectively. Using

Equation (39) we have

$$N_{\text{NSNS}} = T_G \rho_G \sum_{i_1=0}^{1} \sum_{i_2=0}^{1} \mathcal{D}_{i_1 i_2} \mathcal{R} \mathcal{V}_{i_1 i_2}$$

$$= \rho_G \mathcal{R} T_G (\mathcal{D}_{00} \mathcal{V}_{00} + \mathcal{D}_{01} \mathcal{V}_{01} + \mathcal{D}_{10} \mathcal{V}_{10} + \mathcal{D}_{11} \mathcal{V}_{11})$$

$$= (\rho_G \mathcal{R}) (T_G D_1 D_2) V_2,$$
(40)

where $\mathcal{D}_{i_1i_2}$ and $\mathcal{V}_{i_1i_2}$ are given by

$$\mathcal{D}_{i_1 i_2} = \prod_{k=1}^{2} \left[D_k^{i_k} (1 - D_k)^{1 - i_k} \right]$$

$$= D_1^{i_1} (1 - D_1)^{1 - i_1} D_2^{i_2} (1 - D_2)^{1 - i_2}, \tag{41}$$

$$\mathcal{V}_{i_1 i_2} = \begin{cases} V_2 & \text{for } (i_1, i_2) = (1, 1), \\ 0 & \text{for } (i_1, i_2) = (1, 0), (0, 1), (0, 0). \end{cases}$$
(42)

Similarly, the number N_C of coincident events detectable by at least two GW detectors and an EM detector is obtained using $\mathcal{D}_{i_1\cdots i_N}$ and N(z) in Equation (5). If an EM detector with duty cycle factor $D_{\rm EM}$ and field of view $f_{\rm EM}$ is observing at the same time of m detectors in the GW network, the number of observable SGRB events per year up to z by the EM detector is given by $f_{\rm EM}N(z)/(fT_o)$ and the fraction of the observation time is $T_GD_{i_k\cdots i_N}D_{\rm EM}$. The local rate densities of SGRBs that are produced by NSNS and NSBH mergers are given by

$$\rho_{S \text{ NSNS}} = \Gamma_{\text{NSNS}} \mathcal{R} \rho_G, \tag{43}$$

$$\rho_{\text{S.NSBH}} = \Gamma_{\text{NSBH}} (1 - \mathcal{R}) \rho_G, \tag{44}$$

where Γ_{NSNS} and Γ_{NSBH} are the fraction of NSNS and NSBH that produce SGRBs, respectively. The fraction of SGRBs that are produced by NSNS mergers is

$$\mathcal{P} = \frac{\rho_{S, \text{NSNS}}}{\rho_S} = \frac{\Gamma_{\text{NSNS}} \mathcal{R}}{\Gamma_{\text{NSNS}} \mathcal{R} + \Gamma_{\text{NSBH}} (1 - \mathcal{R})},$$
 (45)

where $\rho_S = \rho_{S, \text{NSNS}} + \rho_{S, \text{NSBH}}$ is the total SGRB local rate density. The number N_C of coincident events detectable by at least two GW detectors and the EM detector is

$$N_{C} = \sum_{i_{1}=0}^{1} \cdots \sum_{i_{N}=0}^{1} \{ (T_{G} D_{i_{1}\cdots i_{N}} D_{EM})$$

$$\times \left[\mathcal{P} \frac{f_{EM} N(\mathcal{Z}_{i_{1}\cdots i_{N}})}{f T_{o}} + (1-\mathcal{P}) \frac{f_{EM} N(\mathcal{Y}_{i_{1}\cdots i_{N}})}{f T_{o}} \right] \right\}$$

$$= \frac{T_{G} D_{EM} f_{EM}}{f T_{o}} \sum_{i_{1}=0}^{1} \cdots \sum_{i_{N}=0}^{1} \{ \mathcal{D}_{i_{1}\cdots i_{N}} [\mathcal{P} N(\mathcal{Z}_{i_{1}\cdots i_{N}}) + (1-\mathcal{P}) N(\mathcal{Y}_{i_{1}\cdots i_{N}})] \}.$$

$$(46)$$

The number of events detectable with only a single GW detector in coincidence with an EM detector can be obtained by setting $\mathcal{Z}_{i_1...i_{\mathcal{N}}}$ and $\mathcal{Y}_{i_1...i_{\mathcal{N}}}$ to the largest single-detector NSNS and NSBH search redshifts, respectively.

ORCID iDs

Kentaro Mogushi https://orcid.org/0000-0003-3746-2586

References

```
Abbott, B. P., Abbott, R., Abbott, T. D., et al. 2016, ApJL, 832, L21
Abbott, B. P., Abbott, R., Abbott, T. D., et al. 2017a, PhRvL, 119, 161101
Abbott, B. P., Abbott, R., Abbott, T. D., et al. 2017b, ApJL, 848, L13
Abbott, B. P., Abbott, R., Abbott, T. D., et al. 2017c, ApJ, 839, 12
Abbott, B. P., Abbott, R., Abbott, T. D., et al. 2018, LRR, 21, 3
Abbott, B. P., Abbott, R., Abbott, T. D., et al. 2019, PhRvX, 9, 011001
Alexander, K. D., Margutti, R., Blanchard, P. K., et al. 2018, ApJL, 863, L18
Andreon, S., Cuillandre, J.-C., Puddu, E., & Mellier, Y. 2006, MNRAS,
Atwood, W. B., Abdo, A. A., Ackermann, M., et al. 2009, ApJ, 697, 1071
Band, D., Matteson, J., Ford, L., et al. 1993, ApJ, 413, 281
Barthelmy, S. D., Barbier, L. M., Cummings, J. R., et al. 2005, SSRv, 120, 143
Belczynski, K., Bulik, T., Dominik, M., et al. 2011, arXiv:1106.0397
Belczynski, K., Dominik, M., Bulik, T., et al. 2010, ApJL, 715, L138
Beniamini, P., Petropoulou, M., Barniol, D. R., & Giannios, D. 2019, MNRAS,
   483, 840
Berger, E. 2010, ApJ, 722, 1946
Berger, E. 2013, ApJ, 765, 121
Berger, E., Fox, D. B., Price, P. A., et al. 2007, ApJ, 664, 1000
Bhattacharya, M., Kumar, P., & Smoot, G. 2018, arXiv:1809.00006
Bloom, J. S., Fox, D., Tanvir, N. R., et al. 2009, GCN, 9137, 1
Bloom, J. S., Frail, D. A., & Sari, R. 2001, ApJ, 121, 2879
Branchesi, M., Ligo Scientific Collaboration; Virgo Collaboration, et al. 2012,
   JPhCS, 375, 062004
Burns, E., Connaughton, V., Zhang, B. B., et al. 2016, ApJ, 818, 110
Campana, S., Mangano, V., Blustin, A. J., et al. 2006, Natur, 442, 1008
Cenko, S. B., Berger, E., Nakar, E., et al. 2008, arXiv:0802.0874
Champion, D. J., Lorimer, D. R., McLaughlin, M. A., et al. 2004, MNRAS,
Chruslinska, M., Belczynski, K., Klencki, J., & Benacquista, M. 2018,
   MNRAS, 474, 2937
Cole, S., Norberg, P., Baugh, C. M., et al. 2001, MNRAS, 326, 255
Coward, D., Howell, E. J., Piran, T., et al. 2012, MNRAS, 425, 1365
de Freitas Pacheco, J. A., Regimbau, T., Vincent, S., & Spallicci, A. 2006,
   IJMPD, 15, 235
Dominik, M., Belczynski, K., Fryer, C., et al. 2012, ApJ, 759, 52
Fardal, M. A., Katz, N., Weinberg, D. H., & Romeel, D. 2007, MNRAS,
Fong, W., Berger, E., Blanchard, P. K., et al. 2017, ApJL, 848, L23
Fong, W., & Chornock, R. 2016, GCN, 20168, 1, https://gcn.gsfc.nasa.gov/
   other/161104A.gcn3
Fong, W. F., Berger, E., Chornock, R., et al. 2011, ApJ, 730, 26
Fong, W. F., Berger, E., Chornock, R., et al. 2013, ApJ, 769, 56
Fong, W. F., Berger, E., Margutti, R., & Zauderer, B. A. 2015, ApJ, 815, 102
Fong, W. F., Margutti, R., Chornock, R., et al. 2016, ApJ, 833, 151
Fox, D. B. 2009, GCN, 9134, 1
Fox, D. B., & Ofek, E. 2007, GCN, 6819, 1
Frederiks, D. D. 2013, ApJ, 779, 151
Fruchter, A. S., Levan, A. J., Strolger, L., et al. 2006, Natur, 441, 463
Gehrels, N., Chincarini, G., Giommi, P., et al. 2004, ApJ, 611, 1005
Goldstein, A., Veres, P., Burns, E., et al. 2017, ApJL, 848, L14
Granot, J. 2007, Rev. Mex. Astron. Astrof. Ser. Conf., 27, 140
Guelbenzu, A. N., Klose, S., Greiner, J., et al. 2012, A&A, 548, A101
Guetta, D., & Piran, T. 2006, A&A, 453, 823
Gupte, N., & Bartos, I. 2018, arXiv:1808.06238
Hernquist, L., & Springel, V. 2003, MNRAS, 341, 1253
Hjorth, J., Sollerman, J., Møller, P., et al. 2003, Natur, 423, 847
Hogg, D. W. 1999, arXiv:astro-ph/9905116
Hopkins, A. M., & Beacom, J. F. 2006, ApJ, 651, 142
Howell, E. J., Ackley, K., Rowlinson, A., & Coward, D. 2018, MNRAS, 485, 1435
Jin, Z. P. 2017, ApJ, 857, 128
Kalogera, V., Belczynski, K., Kim, C., et al. 2007, PhR, 442, 75
Kouveliotou, C., Meegan, C. A., Fishman, G. J., et al. 1993, ApJL, 413, L101
Kumar, P., & Granot, J. 2003, ApJ, 591, 1075
Lazzati, D., Perna, R., Morsony, B. J., et al. 2018, PhRvL, 120, 241103
Lee, W. H., Ramirez-Ruiz, E., & Page, D. 2004, ApJL, 608, L5
Leibler, C. N., & Berger, E. 2010, ApJ, 725, 1202
Levan, A. J., Wiersema, K., Tanvir, N. R., Malesani, D., Xu, D., & Postigo, A. d. U.
   2016, GCN, 19846, 1, https://gcn.gsfc.nasa.gov/other/160821B.gcn3
Lien, A., Sakamoto, T., Barthelmy, S. D., et al. 2016, ApJ, 829, 7
Mandel, I., Kelley, L. Z., & Ramirez-Ruiz, E. 2012, in IAU Symp. 285, New
   Horizons in Time Domain Astronomy, ed. R. E. M. Griffin, R. J. Hanisch, &
   R. Seaman (Cambridge: Cambridge University Press), 358
Margutti, R., Berger, E., Fong, W., et al. 2012, ApJ, 756, 63
```

```
Margutti, R., Alexander, K. D., Xie, X., et al. 2018, ApJL, 856, L18
Meszaros, P., & Gehrels, N. 2012, RAA, 12, 1139
Mooley, K. P., Deller, A. T., Gottlieb, O., et al. 2018, Natur, 561, 355
Myers, J. D. 2017, The Swift Technical Handbook v.14, https://swift.gsfc.
  nasa.gov/proposals/tech_appd/swiftta_v14.pdf
Myers, J. D. 2018, The Neil Gehrels Swift Observatory Data Center Archive,
  http://swift.gsfc.nasa.gov/archive/grb_table.html/
Nicuesa Guelbenzu, A., Klose, S., Palazzi, E., et al. 2015, A&A, 583, A88
Nitz, A. H., Dent, T., Canton, T., et al. 2017, ApJ, 849, 118
O'Brien, P. T., & Tanvir, N. R. 2009, GCN, 9136, 1
O'Shaughnessy, R., Kalogera, V., & Belczynski, K. 2010, ApJ, 716, 615
Patrignani, C., Agashe, K., Aielli, G., et al. 2016, ChPhC, 40, 100001
Perley, D. A., Modjaz, M., Morgan, A. N., et al. 2012, ApJ, 758, 122
Pescalli, A., Ghirlanda, G., Salafia, O. S., et al. 2015, MNRAS, 447, 1911
Petrillo, C. E., Dietz, A., & Cavaglià, M. 2012, ApJ, 767, 140
Porciani, C., & Madau, P. 2001, ApJ, 548, 522
Postigo, A. de Ugarte., Thöne, C. C., Rowlinson, A., et al. 2014, A&A, 563, A62
```

```
Privitera, S., Mohapatra, S. R. P., Ajith, P., et al. 2017, PhRvD, 89, 024003
Regimbau, T., Siellez, K., Meacher, D., et al. 2015, ApJ, 799, 69
Rhoads, J. E. 1999, ApJ, 525, 737
Rossi, E., Lazzati, D., & Rees, M. J. 2002, MNRAS, 332, 945
Rowlinson, A., Wiersema, K., Levan, A. J., et al. 2010, MNRAS, 408, 383
Sakamot, T., Troja, E., Aoki, K., et al. 2013, ApJ, 766, 41
Siellez, K., Boër, M., & Gendre, B. 2014, MNRAS, 437, 649
Siellez, K., Boer, M., Gendre, B., et al. 2017, arXiv:1606.03043
Spergel, D. N., Bean, R., Dorè, O., et al. 2007, ApJS, 170, 377
Stone, N., Loeb, A., & Berger, E. 2013, PhRvD, 87, 084053
Voss, R., & Tauris, T. M. 2003, MNRAS, 342, 1169
Wanderman, D., & Piran, T. 2015, MNRAS, 448, 3026
Wilkins, S. M., Trentham, N., & Hopkins, A. M. 2008, MNRAS, 385,
Woosley, S. E., & Bloom, J. S. 2006, ARA&A, 44, 507
Zhang, B., & Meszaros, P. 2002, ApJ, 571, 876
Zhang, B., & Meszaros, P. 2004, IJMPA, 19, 2385
```